scientific reports

Check for updates

OPEN

Microstructural and microvascular features of white matter hyperintensities and their association with small vessel disease markers

Lily L. Wang[1], Brady J. Williamson[1], Bin Zhang[2], Aakanksha Sriwastawa[1], Yasmin N. Aziz[3], Eleni Antzoulatos[4], Cody B. Stephens[1], Achala Vagal[1], Pooja Khatri[3] & Mark W. DiFrancesco[1,5]✉

White matter hyperintensities (WMH) are the most prominent imaging feature of small vessel disease (SVD). WMH and other imaging features of SVD are likely the result of ongoing insults associated with cognitive decline and cerebrovascular events. Emerging evidence suggests degradation of the neurovascular unit may underlie the pathogenesis of SVD. This prospective pilot study employed MRI in 19 subjects (68.2 ± 11.5 years of age) for diffusion-weighted imaging, applied to intravoxel incoherent motion (IVIM) modeling, to characterize microstructural and microvascular properties throughout the brain and arterial spin labeling, using multiple labeling and delay times, to measure dynamic perfusion properties including blood–brain barrier permeability (PS) in gray matter (GM). IVIM revealed WMH to have significantly greater blood volume fraction and lower pseudodiffusion and bulk diffusion than normal-appearing white matter (NAWM). IVIM parameters and PS, in canonical GM network regions, correlated with WMH volume with at least moderate effect size. Findings suggest the potential for neovascularization and evidence of restricted diffusion in WMH compared to surrounding NAWM. Regional changes in GM pertaining to the NVU scale in proportion to WMH load. Observed GM changes precede visible MR imaging abnormalities. Their early detection could elucidate SVD mechanisms of brain injury and inform future preventative measures.

Keywords Small Vessel Disease, Arterial spin labeling, Diffusion-weighted imaging, Blood–brain-barrier, Brain microvasculature, White matter hyperintensities

Cerebral small vessel disease (SVD) refers to a syndrome of clinical and imaging findings that are thought to result from pathologies in perforating cerebral arterioles, capillaries, and venules. Despite the latest advances in medicine and technology, SVD is associated with 25% of the 15 million annual strokes worldwide and about 45% of dementias.[1] SVD is seen routinely on conventional MRI sequences, characterized by white matter hyperintensities (WMH), lacunar infarcts, cerebral microbleeds, dilated perivascular spaces, and atrophy[2–4]. More expansively, SVD is a dynamic disease with whole-brain impact that often accumulates subclinically.[5] Visible lesions likely reflect the end of a cascade of damages.[6]

Among the SVD imaging features, WMH are of particular interest to clinical and research communities due to their associative, and possibly causative, role in cognitive decline, incident stroke, stroke severity, and potential for recovery[7,8].

Currently known vascular risk factors and standard clinical imaging cannot explain the variance in SVD development and progression.[9] There is also limited information about the precursors of visible imaging markers

[1]Department of Radiology, University of Cincinnati College of Medicine, Cincinnati, OH, USA. [2]Division of Biostatistics and Epidemiology, Cincinnati Children's Hospital Medical Center, Cincinnati, OH, USA. [3]Department of Neurology and Rehabilitation Medicine, University of Cincinnati College of Medicine, Cincinnati, OH, USA. [4]Department of Neurology, Emory University School of Medicine, Atlanta, GA, USA. [5]Department of Radiology, Cincinnati Children's Hospital Medical Center, ML5033, Cincinnati, OH 45243, USA. ✉email: mark.difrancesco@cchmc.org

like WMH and whether these pathological changes are reversible. Conventional imaging does not fully explain tissue changes prior to the development of overt disease.[4]

Accumulating evidence suggests a pivotal role of neurovascular unit degradation including microvascular changes contributing to blood–brain barrier compromise and ultimately the pathogenesis of SVD.[3,10] Currently, the most studied modality to measure BBB permeability is dynamic contrast-enhanced magnetic resonance imagining (DCE-MRI). Unfortunately, DCE-MRI has distinct challenges, including the need for exogenous contrast administration, low spatial resolution, computational complexity, and lack of agreed standards.[11–14]

Novel MRI techniques that do not rely on contrast with the potential to detect early functional and microstructural changes in the neurovascular unit are needed to narrow the gap between SVD-related alterations that are not visible on conventional MRI and visible SVD-related features such as WMH. Two such promising techniques are intravoxel incoherent motion (IVIM) imaging and arterial spin labelling (ASL).

IVIM is measured using diffusion-weighted MRI assessing both parenchymal microstructure and microvascular topology based on pseudodiffusion representing incoherent flow of water molecules in microvessels. IVIM metrics have been shown to correlate with cerebral blood flow and perfusion in acute ischemic stroke patients.[15] ASL, often used to measure baseline cerebral perfusion by magnetically tagging water in the blood as it enters the brain, has also been applied to dynamically capture the inflow and exchange of tagged blood using a two-compartment model that distinguishes intravascular "blood water" from extravascular "tissue water" to deduce regional BBB permeability.[16]

The aims of our prospective pilot study were to utilize the IVIM technique to assess regional microstructural and microvascular integrity in white matter of SVD patients and then assess global impact associated with WMH burden by employing both IVIM and pCASL measures, including BBB permeability, in cortical regions of those patients. We hypothesized that microstructural and microvascular alterations would be detected in WMH and in normal-appearing tissue surrounding WMH. BBB permeability in gray matter was expected to increase in proportion to WMH load, indicating a relationship between clinical imaging indicators of SVD burden and global vascular compromise.

Results

Study participants

Nineteen patients with varying WMH loads between the ages of 37 and 84 years (mean ± SD: 68.2 ± 11.5 years), including 6 (31.6%) females, were enrolled. One patient was unable to complete the MRI. Diffusion-weighted imaging (DWI) was successfully acquired for 16 patients and 14 patients successfully completed both DWI and pseudocontinuous arterial spin labeling (pCASL) acquisitions. The patients varied with respect to cardiac health and cardiovascular risk factors. Demographic and clinical details are provided in Table 1.

Characteristic	All patients enrolled (N = 19)	Analyzed for DWI of WMH (N = 16)	Analyzed for ASL and DWI of GM (N = 14)
Age (mean ± SD years)	68.2 ± 11.5	71.3 ± 7.9	71.4 ± 8.4
Sex	6 F, 13 M	5 F, 11 M	5 F, 9 M
Race	2 AA, 17 White	2 AA, 14 White	2 AA, 12 White
Fazekas, periventricular	1.61 ± 0.92*	1.56 ± 0.96	1.57 ± 1.02
Fazekas, deep	1.67 ± 0.59*	1.69 ± 0.60	1.64 ± 0.63
Fazekas, total	3.28 ± 1.27*	3.25 ± 1.34	3.21 ± 1.42
WMH volume [cc]	7.29 ± 8.99*	6.48 ± 9.08	6.39 ± 9.59
Hispanic Ethnicity	0	0	0
Hypertension	11	10	9
Hyperlipidemia	11	10	8
Diabetes Mellitus	3	3	2
Carotid Stenosis	3	2	2
Coronary Artery Disease	6	5	3
Atrial Fibrillation	1	1	1
Heart Failure	1	1	1
Dementia	4	4	4
Chronic Kidney Disease	2	2	1
Prior Stroke	1	0	0
Steroid Use	0	0	0
Obstructive Sleep Apnea	7	7	5
Current Smoker	4	2	2
Prior Neurosurgery	1	1	1

Table 1. Patient Characteristics. WMH = white matter hyperintensity, DWI = diffusion-weighted imaging, ASL = arterial spin labeling, GM = gray matter, F = female, M = male, AA = African American, SD = standard deviation. * excluding one patient who did not complete MRI.

IVIM Parameter	Regional Comparison (mean difference ± SD)	p-value (FDR)
vbw	WMH > Peri-WMH* (0.045 ± 0.031)	< 0.001
	Peri-WMH > NAWM* (0.050 ± 0.029)	< 0.001
	WMH > NAWM* (0.095 ± 0.032)	< 0.001
D*	WMH vs. Peri-WMH (-3.0e-4 ± 7.0e-4)	0.328
	Peri-WMH < NAWM* (-1.4e-3 ± 7.6e-4)	< 0.001
	WMH < NAWM* (-1.7e-3 ± 1.2e-3)	< 0.001
D	WMH vs. Peri-WMH (1.1e-5 ± 3.5e-5)	0.434
	Peri-WMH < NAWM* (-5.2e-5 ± 4.7e-5)	0.003
	WMH < NAWM* (-6.3e-5 ± 7.1e-5)	0.011
D* x vbw	WMH > Peri-WMH* (1.7e-4 ± 9.8e-5)	< 0.001
	Peri-WMH vs. NAWM (-3.4e-6 ± 1.0e-4)	0.89
	WMH > NAWM* (1.7e-4 ± 1.6e-4)	0.003

Table 2. Regional WM comparisons of IVIM parameters. WM = white matter, IVIM = intravoxel incoherent motion, vbw = blood volume fraction, D = bulk tissue diffusion coefficient, D* = pseudodiffusion coefficient (due to flow in microvessels), D* x vbw = product reflecting blood flow, WMH = white matter hyperintensity region, Peri-WMH = 4 mm thick white matter region surrounding WMH, NAWM = normal-appearing white matter excluding WMH and Peri-WMH, p-value is for one-sample t-test of regional comparisons among patients, FDR-corrected: * indicates statistical significance at $p < 0.05$. Diffusion units are in mm2/s.

Parameter	Cohen's f^2	Dependence on WMH vol	Network	Anatomic Region (MNI coord.)
vbw	0.23	negative	DMN	Left Lateral Parietal (– 39,– 77,33)
	0.24	negative	SMN	Left Lateral (– 55,– 12,29)
	0.28	positive	VIS	Occipital (0,– 93,– 4)
	0.27	positive	SAL	Right Anterior Insula (47,14,0)
	0.32	negative	SAL	Left SMG (– 60,– 39,31)
	0.23	negative	LAN	Left pSTG (– 57,– 47,15)
	0.23	negative	CER	Anterior (0,– 63,– 30)
D	0.18	negative	SAL	Left Anterior Insula (– 44,13,1)
	0.35	positive	LAN	Left pSTG (– 57,– 47,15)
	0.26	negative	CER	Posterior (0,– 79,– 32)
D*	0.43	positive	DMN	Left Lateral Parietal (– 39,– 77,33)
	0.15	negative	SAL	Left Anterior Insula (– 44,13,1)
	0.27	positive	CER	Anterior (0,– 63,– 30)

Table 3. Correlations of cortical IVIM parameters with WMH volumes (Cohen's $f^2 > 0.15$). IVIM = intravoxel incoherent motion, WMH = white matter hyperintensity, vbw = blood volume fraction, D = bulk tissue diffusion coefficient, D* = pseudodiffusion coefficient (due to flow in microvessels), DMN = default mode network, SMN = sensorimotor network, VIS = visual network, SAL = salience network, LAN = language network, CER = cerebellar network, SMG = supramarginal gyrus, pSTG = posterior superior temporal gyrus.

IVIM parameters in white matter

The blood volume fraction, vbw, was found to be significantly greater on average in WMH than in peri-WMH zones, while vbw in peri-WMH was significantly greater than in NAWM. While pseudodiffusion, D*, was not significantly different between WMH and surrounding tissue, these zones had significantly lower D* than NAWM. The same relative regional relationships were observed for bulk diffusion, D. The flow-related product, vbw x D*, was found to be significantly elevated in WMH vs. peri-WMH zones, while a statistically significant difference between peri-WMH and NAWM could not be discerned (see Table 2).

IVIM parameters in cortical gray matter regions

Regression of IVIM parameters in gray matter regions to WMH volume failed to result in a statistically significant WMH coefficient for any IVIM parameter in any region. This may have been due to our modest sample size. Therefore, in acknowledgment of the possibility of false negatives and in order to set targets for larger future studies, we expressed regression results for the WMH volume coefficient as effect size represented as Cohen's f^2, reporting outcomes with f^2 exceeding 0.15, considered to be a moderate threshold[17].

Table 3 details the network regions with WMH volume terms for each IVIM parameter with $f^2 > 0.15$. The default mode and cerebellar networks show increased pseudodiffusion and decreased blood volume fraction with increases in WMH load. Conversely, WMH load is negatively associated with pseudodiffusion and positively

associated with blood volume fraction for insular components of the salience network. Posterior elements of the salience network, the sensorimotor network, and the language network also displayed negative association of blood volume fraction with WMH load. The behavior of bulk diffusion mirrored pseudodiffusion for the same insular portion of the salience network, but these terms had opposite dependence on WMH load between the anterior and posterior parts of the cerebellar network.

pCASL parameters in cortical gray matter regions

Association of pCASL parameters with WMH load was also reported as effect size, as described for the IVIM parameters. The pCASL model parameters depended on WMH volume in numerous network regions with moderate ($f^2 > 0.15$) and, in some cases, large ($f^2 > 0.35$) effect sizes (Table 4). The BBB permeability, PS, had a negative dependence on WMH load in default mode, sensorimotor, and visual regions, and positive dependence for the frontal portion of the dorsal attention network. The salience network components had mixed dependencies on WMH load; negative frontally in the anterior cingulate gyrus, but positive in the supramarginal gyrus posteriorly. Interestingly, the left and right anterior insula had opposing associations of PS with WMH load. With only the exception of the left frontal eye field of the dorsal attention network, the arterial transit time, tex, the arrival time, tA, the tissue longitudinal relaxation rate, R1t, and the coefficient proportional to flow, CBFp, all have positive dependence on WMH load. This pattern was especially widespread for tA and R1t.

Discussion

This prospective pilot study characterized regional white matter and gray matter microstructural and microvascular properties in SVD using novel IVIM and ASL techniques. The advantage of using ASL and IVIM is that both non-contrast MR techniques can investigate regional disruption of the neurovascular unit that we hypothesize to underlie pathogenesis of SVD.[10]

We found significant differences in mean IVIM parameters between WMH, tissue immediately surrounding WMH, and remaining NAWM. Increases in vascular density (vbw) coupled with decreases in both pseudodiffusion (D*) and bulk diffusion (D), suggest an environment of structural disruption in WMH zones with augmentation of highly ramified microvessels[18]. The latter is a potential signature of neovascularization. These findings mostly align with prior work using IVIM imaging that found increased vascular density and decreased pseudodiffusion in periventricular WMH compared to NAWM in SVD[19–21]. One of these studies, however, reported an increase in bulk diffusion in the periventricular zone[19]. Another recent study employing IVIM in SVD only reported bulk diffusion, finding increased D in WMH compared to NAWM[22]. Our contrasting result for bulk diffusion in WMH may be due to differences in methodology or location of WMH between studies, but our finding of decreased D in the context of potential neovascularization is consistent with prior investigations of tumor microenvironments[23]. We found an abrupt increase in the perfusion-related product vbw x D* in WMH zones on average, conflicting with some prior studies that reported reduced blood flow in WMH using other MRI methods[24–27]. However, the product vbw x D* only reflects the potential for blood flow and a more nuanced interpretation of the product might be considered for WMH. The observed combination of apparent increase in blood volume (vbw) and decreased pseudodiffusion (D*) may predominantly reflect an increase in highly tortuous and ramified microvessels, with abnormal flow properties compared to native vessels[28]. Several studies of SVD have indicated increased tortuosity of brain microvessels[29–31]. Indeed, these aberrant vessels may be associated with resultant damages such as lacunar infarctions, hemorrhage and dementia.[1]

Indications of global impact of WMH were observed in our study. IVIM parameters were associated with SVD severity, expressed as WMH volume, in canonical network regions of gray matter with at least moderate effect size. We observed in our study that increased WMH volume associated with increased pseudodiffusion coupled with decreased blood volume fraction in the default mode and cerebellar networks, suggesting simplification of the microvascular tree due to the depletion of microvessels. This is in opposition to our findings in and around WMH outlined above. Loss of blood volume with increased WMH load was apparent in other brain networks as well in our study, but without a corresponding discernible pseudodiffusion increase. The opposite trend of increasing blood volume fraction and decreasing pseudodiffusion with increasing WMH burden was observed in our study in anterior insula segments of the salience network, suggesting proliferation, similar to our findings in WMH. Trends in microvascular integrity observed in and near WMH appear to extend to gray matter regions, but with some gray matter regions showing evidence of microvascular depletion rather than proliferation. We speculate that this indicates different stages of disease manifestation in gray matter that could be elucidated by longitudinal studies using IVIM.

We also explored the relationship between WMH burden (total volume) and regional gray matter vascular properties, including BBB permeability, derived from a dynamic blood flow model applied to pCASL data. BBB permeability varied in dependence on WMH load among canonical network regions of gray matter, with some regions increasing permeability, suggesting a leaky BBB, and some showing diminished permeability with increasing WMH load. A leaky BBB could be the cause and/or the result of ischemia, inflammation and altered immune response[32]. While SVD is most often associated with the breakdown of the BBB manifested as increased permeability in WMH, NAWM, or gray matter[22,33,34], this has not been a universal finding in other studies. Some recent studies have reported decreased exchange rate of the BBB in association with SVD[34,35]. Li et al. recently applied a diffusion-prepared pCASL approach to patients with hereditary forms of SVD finding decreases in blood water exchange rate across the BBB[36]. This was interpreted as dysfunction of aquaporin channels at the microvessels reflecting diminished ability to clear waste; a potential physiological mechanism for SVD[36]. Our study did not include hereditary forms of SVD, yet hereditary SVD has been employed as a model for sporadic or age-related SVD[37]. Methods to measure BBB permeability that are based on water exchange, like the one used in this study, may characterize multiple forms of BBB functionality. The regional gray matter variation in the dependence of BBB permeability on WMH burden observed in this study may indicate multiple

Parameter	Cohen's f^2	Dependence on WMH vol	Network	Anatomic Region (MNI coord.)
PS	0.29	negative	DMN	Left Lateral Parietal (-39,-77,33)
	0.18	negative	SMN	Right Lateral (56,-10,29)
	0.20	negative	VIS	Left Lateral (-37,-79,10)
	0.16	negative	SAL	ACC (0,22,35)
	0.52	negative	SAL	Left Anterior Insula (-44,13,1)
	0.32	positive	SAL	Right Anterior Insula (47,14,0)
	0.23	positive	SAL	Left SMG (-60,-39,31)
	0.37	positive	DAN	Left FEF (-27,-9,64)
tex	0.17	positive	DMN	Right Lateral Parietal (47,-67,29)
	0.31	positive	SAL	Left RPFC (-32,45,27)
	0.26	negative	DAN	Left FEF (-27,-9,64)
	0.54	positive	FPN	Left LPFC (-43,33,28)
	0.15	positive	LAN	Right pSTG (59,-42,13)
	0.16	positive	CER	Anterior (0,-63,-30)
tA	0.31	positive	DMN	PCC (1,-61,38)
	0.26	positive	SMN	Left Lateral (-55,-12,29)
	0.25	positive	SMN	Right Lateral (56,-10,29)
	0.22	positive	VIS	Medial (2,-79,12)
	0.43	positive	SAL	ACC (0,22,35)
	0.16	positive	SAL	Left Anterior Insula (-44,13,1)
	0.35	positive	SAL	Right Anterior Insula (47,14,0)
	0.27	positive	SAL	Left RPFC (-32,45,27)
	0.41	positive	SAL	Right RPFC (32,46,27)
	0.27	positive	SAL	Left SMG (-60,-39,31)
	0.63	positive	SAL	Right SMG (62,-35,32)
	0.21	negative	DAN	Left FEF (-27,-9,64)
	0.17	positive	DAN	Left IPS (-39,-43,52)
	0.19	positive	DAN	Right IPS (39,-42,54)
	0.52	positive	FPN	Right LPFC (41,38,30)
	0.61	positive	FPN	Right PPC (52,-52,45)

Continued

Parameter	Cohen's f^2	Dependence on WMH vol	Network	Anatomic Region (MNI coord.)
R1t	0.51	positive	DMN	MPFC (1,55,-3)
	0.21	positive	DMN	Left Lateral Parietal (-39,-77,33)
	0.28	positive	SMN	Left Lateral (-55,-12,29)
	0.40	positive	SMN	Right Lateral (56,-10,29)
	1.18	positive	SMN	Superior (0,-31,67)
	0.57	positive	VIS	Lateral (38,-72,13)
	0.33	positive	SAL	ACC (0,22,35)
	0.64	positive	SAL	Left RPFC (-32,45,27)
	0.15	positive	SAL	Left SMG (-60,-39,31)
	0.59	positive	SAL	Left SMG (-60,-39,31)
	0.88	positive	DAN	Right FEF (30,-6,64)
	0.21	positive	DAN	Left IPS (-39,-43,52)
	0.21	positive	DAN	Right IPS (39,-42,54)
	0.31	positive	FPN	Left LPFC (-43,33,28)
	0.29	positive	FPN	Right PPC (52,-52,45)
	1.60	positive	LAN	Left IFG (-51,26,2)
	0.47	positive	LAN	Left pSTG (-57,-47,15)
	0.33	positive	LAN	Right pSTG (59,-42,13)
	0.53	positive	CER	Posterior (0,-79,-32)
CBFp	0.37	positive	SAL	Left RPFC (-32,45,27)
	0.15	negative	DAN	Left FEF (-27,-9,64)
	0.19	positive	DAN	Right FEF (30,-6,64)

Table 4. Correlations of cortical ASL parameters with WMH volumes (Cohen's $f^2 > 0.15$). ASL = arterial spin labeling, WMH = white matter hyperintensity, PS = BBB permeability/surface area product, tex = arterial transit time, tA = time of arrival, R1t = tissue R1, CBFp = cerebral blood flow factor, DMN = default mode network, SMN = sensorimotor network, VIS = visual network, SAL = salience network, DAN = dorsal attention network, FPN = fronto-parietal network, LAN = language network, CER = cerebellar network, ACC = anterior cingulate cortex, SMG = supramarginal gyrus, FEF = frontal eye field, RPFC = rostral prefrontal cortex, LPFC = lateral prefrontal cortex, pSTG = posterior superior temporal gyrus, PCC = posterior cingulate cortex, IPS = intraparietal sulcus, PPC = posterior parietal cortex, MPFC = medial prefrontal cortex.

pathophysiological mechanisms of SVD at play[38]. Other parameters derived from the pCASL data, such as arterial transit time, tex, time of arrival of labeled blood, tA, and tissue R1 predominantly increased across gray matter regions with increasing WMH burden. Delays in arrival time in proportion to disease severity appear to be consistent in the context of SVD[33,39]. Delays in arrival time and arterial transit time may suggest that pathophysiological mechanisms of SVD resulting in WMH extend to having a negative global impact on brain vasculature. Similarly, widespread increases in cortical R1 related to WMH load may be indicative of tissue structural degradation[40]. Measures of R1 in SVD are not commonly reported, but one small study[39] found, contrary to our findings, decreased gray matter R1 in SVD patients, offering the explanation that it might be due to impaired tissue clearance. Further multiparametric relaxometry investigations in SVD may advance understanding of resultant tissue microstructural changes.

Our pilot study has multiple limitations, including a small number of subjects and lack of a control group. The small sample size coupled with challenging signal-to-noise levels of our imaging techniques necessitated use of regional parameter assessments and expression of some results as effect size. Nevertheless, identification of at least moderate effect sizes serves to form hypotheses and identify regional targets for future imaging studies of SVD. Our choice of covariates in the regression model in gray matter regions was also limited by the sample size. As a result, we did not adjust for multiple variables including sex and race. The resolution of the DWI and pCASL acquisitions and subsequent smoothing during preprocessing resulted in partial volume effects that must be considered when interpreting our gray matter analyses. The WMH on T2/FLAIR MR imaging that we analyzed may have multiple etiologies other than vascular or ischemic. While this study uses WMH load as a surrogate indicator of SVD severity, other SVD MRI markers such as microhemorrhage, enlarged perivascular space, and atrophy could play a role in explaining vascular changes.[2] In addition, this study did not distinguish WMH according to location (periventricular vs. deep) in the analysis. A larger study could pursue the interesting question of location dependence of WMH tissue properties and their global impact. It should also be pointed out that our IVIM and pCASL analyses and their interpretation depend on unvalidated tissue and vascular models. Further research relating imaging and clinical and functional outcome would have an impact on patient prognosis and treatment.

In conclusion, we applied advanced ASL and IVIM techniques to assess regional microstructural and microvascular integrity in white matter and gray matter in SVD patients. IVIM results in white matter suggest a potential for neovascularization in WMH with gradation into surrounding tissue compared to the

remainder of NAWM. These microvascular changes extended into some gray matter regions in proportion to WMH burden while other regions showed evidence of microvessel depletion. Assessment of dynamic blood flow and exchange in gray matter similarly revealed regional variation in BBB permeability in association with WMH burden. Other key parameters of blood flow dynamics, such as blood arrival time, exhibited increases broadly across gray matter. Our findings suggest that microvascular and microstructural changes evident in WMH and surrounding tissue extend to cortical gray matter. Our results motivate extension of this study with larger sample size and inclusion of healthy controls. The changes observed in zones immediately surrounding WMH and in gray matter precede visible MR imaging abnormalities. Early detection of these changes could help with better understanding of mechanisms of brain injury and preventative measures. The combination of MR techniques and data processing employed in this study can be applied to not just stroke patients, but a wide range of pathologies, such as demyelination, inflammation, and trauma, without the need for the administration of intravenous gadolinium contrast.

Methods

Participants

This is a prospective, observational pilot study. The subjects were recruited at the University of Cincinnati. Inclusion criteria were adult subjects scheduled for an MRI at the University of Cincinnati Gardener Neuroscience Institute. The research MRI sequences were added to the clinical MRI. Subjects with prior neurosurgery, prior brain tumor, current steroid use, inability to undergo an MRI study, recent head trauma, large hemorrhage, degenerative, demyelinating and inflammatory brain diseases were excluded. The subjects were selected to represent a range of WMH load from minimal to severe. The experimental protocol was approved by the Institutional Review Board of the University of Cincinnati (MOD04_2020-0802). Written informed consent was obtained from all participants. All methods were carried out in accordance with the Declaration of Helsinki and relevant guidelines and regulations. The first 19 patients who consented to the study were enrolled. Patient characteristics including age, smoking, hypertension, diabetes, carotid stenosis, coronary arterial disease, atrial fibrillation, heart failure with reduced ejection fraction, dementia, chronic kidney disease, prior stroke, steroid use, and obstructive sleep apnea were collected.

Image acquisition and processing

MRI Protocol

MRI was completed on a GE Architect 3 Tesla scanner using a protocol comprised of 3D structural images including T1-weighted (3D BRAVO, repetition time (TR)/echo time(TE)/inversion time(TI) = 6.6/2.6/450 ms, flip angle = 12), T2-weighted (3D fast spin-echo (FSE), TR/TE = 3000/86 ms), and T2-FLAIR (TR/TE/TI = 6000/102/1777 ms), each acquired with field of view (FOV) = 200 × 200x188 mm with matrix = 192 × 192x192. The structural images were reconstructed with matrix = 512 × 512x376 (voxel size 0.39 × 0.39x0.5 mm) for the T1-weighted and T2-FLAIR, and 256 × 256x376 (voxel size 0.78 × 0.78x0.5) for the T2-weighted volume. The protocol also included a diffusion-weighted imaging (DWI) series with background suppression comprised of 14 image volumes (TR/TE/TI = 9000/70/2200 ms, FOV = 240 × 240x150 mm, matrix = 64 × 64, 30 slices, 5 mm thick), each with a different diffusion weighting (b = 0, 10, 20, 30, 40, 60, 80, 120, 160, 200, 300, 500, 750, 1000 s/mm^2). Each DWI volume was the average of acquisitions along three orthogonal gradient directions. Dynamic perfusion was assessed by a series of pseudocontinuous arterial spin labeling (pCASL) acquisitions (axial spiral, TR/TE = 4592/11.4 ms, 8 arms, 600 points, FOV = 220 mm, 38 slices, 4 mm thick) using 16 combinations of carotid label durations (tau) and post-label delays (PLD) meant to capture the arrival of labeled blood and subsequent tissue exchange in the brain. Four pCASL sequences each captured data for three PLD values, each with tau = 1200 ms, using Hadamard encoding[41] in the GE Enhanced ASL package. An additional set of four sequences each provided data for one PLD value with tau = 700 ms. Due to technical factors, only 13 pCASL timings (tau + PLD times) were applied for analysis: 1000, 1200, 1400, 1650, 1900, 2500, 2800, 3100, 3700, 4000, 4300, 4900, and 5200 ms. The Enhanced ASL package reconstructed and processed the pCASL data to provide a perfusion image for each combination of tau and PLD.

Processing of DWI data

The DWI series underwent realignment with eddy-current correction using the FDT Diffusion Toolbox in FSL (version 6.0, FMRIB Software Library: www.fmrib.ox.ac.uk/fsl). Following coregistration with the b = 0 DWI realigned image, the T1-weighted structural image was processed in SPM12 (version 7771, http://www.fil.ion.ucl.ac.uk/spm/software/spm12/] under the Matlab computing environment (Matlab version 23.2.0 (R2023b), Natick, Massachusetts: The Mathworks, Inc. https://mathworks.com) for segmentation and normalization to MNI space in a combined procedure based on gray matter, white matter, and cerebrospinal fluid priors[42]. The resulting normalization transform was applied to the entire aligned DWI series with 4 mm isotropic voxel size. Finally, the DWI data were smoothed utilizing an 8 mm Gaussian kernel.

Following preprocessing, DWI data were fitted voxel-wise by nonlinear least squares using the lsqcurvefit module in Matlab to the intravoxel incoherent motion (IVIM) model[43] describing the fractional change in signal: S/S0 = (1-vbw)*exp(-bD) + vbw*exp(-b(D + D*)), where b is the b-value for diffusion weighting, vbw is the volume fraction of blood, D is the bulk tissue diffusion coefficient and D* is the pseudodiffusion coefficient representing flow through ramified microvessels. The model generated, for each subject, voxel-wise maps of the three IVIM parameters, vbw, D, and D*, and the product vbw x D*, related to flow. The processed DWI data were also re-gridded in SPM12 to 2 × 2x4 mm resolution for registration and analysis with the pCASL data.

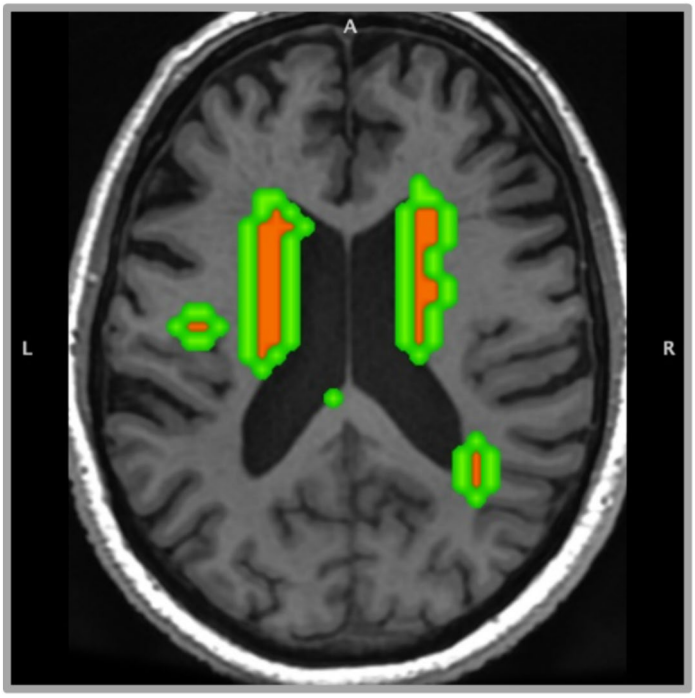

Fig. 1. Example normalized white matter hyperintensity (WMH) regions (red) and peri-WMH zones (green) overlaid on a slice of a T1-weighted image volume.

Processing of pCASL data

Raw perfusion images were first merged into a single four-dimensional file per subject in the order of pCASL timings. SPM12 preprocessing realigned the merged images and coregistered the structural image to the mean realigned image. Segmentation, spatial normalization, and smoothing followed in SPM12 resulting in a normalized pCASL series and gray matter segmentation written with 2 × 2x4 mm voxel size and smoothed with an 8 mm Gaussian kernel. The preprocessing procedure finally applied a gray matter mask to the pCASL series, represented by the gray matter segmentation at the threshold of 25%.

A Matlab script, written in-house, fitted the preprocessed pCASL perfusion signal to the pCASL timings voxel-wise, via the lsqcurvefit nonlinear least squares module, to a four-phase, two-compartment model[16,44]. The model describes evolution of the perfusion signal from arrival of labeled blood to the voxel through transport via arterioles to the capillaries and subsequent exchange with tissue. Parameterization of the model includes an amplitude proportional to the cerebral blood flow (CBFp), the R1 (inverse T1) of the bulk tissue (R1t), the arterial transit time within the voxel (tex), and the capillary permeability per unit surface area (PS) divided by the blood volume fraction. To obtain PS, an indicator of blood–brain-barrier (BBB) permeability, processing included the IVIM parameter value vbw, the blood volume fraction, from the re-gridded maps derived from the DWI data. Details of the model for a similar application to assess the BBB can be found in the Appendix of Gulati et al.[45].

Data analysis

Analysis of IVIM model parameters in white matter

The first analysis of IVIM parameters focused on WMH manually delineated using the T2-FLAIR images and checked by the neuroradiologist (LW). Total WMH was calculated according to this segmentation. We assessed each IVIM parameter: the blood volume fraction, vbw, the bulk diffusion, D, the pseudodiffusion, D*, and the product vbw x D*, proportional to flow, voxel-wise throughout white matter segregated between regions of WMH, 4 mm thick peri-WMH zones, and remaining normal-appearing white matter (NAWM) (see Fig. 1 for an example). Peri-WMH zones were defined by dilating the segmented WMH regions by one voxel. All analyses were restricted to white matter for each patient using the white matter segmentation from preprocessing in SPM12. Differences in mean IVIM parameter values were assessed between regions for each patient. The mean difference between each pair of regions was evaluated by one-sample t-test across patients. A $p < 0.05$ was considered statistically significant after correction for multiple comparisons using false discovery rate.

Analyses of IVIM and pCASL model parameters in gray matter

IVIM parameters were also collected voxel-wise at the re-gridded resolution matching the pCASL data within the gray matter mask described above. Linear regression of the total volume of WMH to mean IVIM parameters within 32 Gy matter regions identified as comprising canonical functional networks explored the association between white matter manifestation of SVD and regional changes in gray matter microvascular and microstructural integrity. We utilized network region masks packaged with the CONN application[46]

derived from independent component analysis of 497 resting-state fMRI datasets from the Human Connectome Project[47]. Each regression included covariates for age and the sum of five cardiovascular risk scores obtained from a medical chart review including yes = 1 and no = 0 for hypertension, hyperlipidemia, diabetes mellitus, prior stroke, and smoking status.

We also explored the potential relationships between cortical vascular properties and WMH load by regressing total WMH volume to the mean of each of the pCASL model parameters; BBB permeability, PS, blood time of arrival, tA, arterial transit time, tex, tissue relaxivity, R1t, and signal amplitude proportional to blood flow, CBFp, within the gray matter canonical network regions, as done for the cortical IVIM parameters, using the same covariates. Statistical significance of the WMH volume term for each regression (using IVIM or pCASL parameters) was defined as false discovery rate corrected p (FDRp) < 0.05.

Statistical analysis

Characteristics of the patients were described, with continuous variables summarized using means and standard deviations (SD) and categorical variables summarized using counts. Mean differences in IVIM parameters between pairs of tissue regions including WMH, peri-WMH and NAWM, were assessed for difference from zero among the patients using one-sample t-tests. Resulting p-values were corrected for multiple comparisons using false discovery rate (FDR). Linear regression was used to assess the relationships between IVIM parameters and pCASL parameters in cortical regions and WMH volumes. A cardiovascular risk score and age were used as covariates. WMH volume coefficients not reaching statistical significance at $p < 0.05$ were described as effect size using Cohen's f^2. Statistical processing was performed in Matlab (Matlab version 23.2.0 (R2023b), Natick, Massachusetts: The Mathworks, Inc. https://mathworks.com).

Author disclosures

Lilly Wang is a central reader for NIH-funded trials: FASTEST, SISTER, and VERIFY. Achala Vagal is a consultant with Cerebra AI.

Data availability

The data that support the findings of this study are not openly available due to reasons of sensitivity and are available from the corresponding author upon reasonable request. Data are located in controlled access data storage at Cincinnati Children's Hospital Medical Center and at the University of Cincinnati.

Received: 23 February 2025; Accepted: 22 May 2025
Published online: 27 May 2025

References

1. Pantoni, L. Cerebral small vessel disease: from pathogenesis and clinical characteristics to therapeutic challenges. *Lancet Neurol.* **9**(7), 689–701 (2010).
2. Mahammedi, A. et al. Small Vessel Disease, a Marker of Brain Health: What the Radiologist Needs to Know. *AJNR Am. J. Neuroradiol.* **43**(5), 650–660 (2022).
3. Wardlaw, J. M., Smith, C. & Dichgans, M. Small vessel disease: mechanisms and clinical implications. *Lancet Neurol.* **18**(7), 684–696 (2019).
4. Wardlaw, J. M. et al. Neuroimaging standards for research into small vessel disease and its contribution to ageing and neurodegeneration. *Lancet Neurol.* **12**(8), 822–838 (2013).
5. Schmidt, W. et al. Train the vessel, gain the brain: physical activity and vessel function and the impact on stroke prevention and outcome in cerebrovascular disease. *Cerebrovasc. Dis.* **35**(4), 303–312 (2013).
6. Zanon Zotin, M. C. et al. Cerebral small vessel disease and vascular cognitive impairment: from diagnosis to management. *Curr. Opin. Neurol.* **34**(2), 246–257 (2021).
7. van der Flier, W. M. et al. Small vessel disease and general cognitive function in nondisabled elderly: the LADIS study. *Stroke* **36**(10), 2116–2120 (2005).
8. Vermeer, S. E. et al. Silent brain infarcts and the risk of dementia and cognitive decline. *N. Engl. J. Med.* **348**(13), 1215–1222 (2003).
9. Wardlaw, J. M. et al. Changes in background blood-brain barrier integrity between lacunar and cortical ischemic stroke subtypes. *Stroke* **39**(4), 1327–1332 (2008).
10. Paschoal, A. M. et al. Intravoxel incoherent motion MRI in neurological and cerebrovascular diseases. *Neuroimage Clin.* **20**, 705–714 (2018).
11. Thrippleton, M. J. et al. Quantifying blood-brain barrier leakage in small vessel disease: Review and consensus recommendations. *Alzheimers Dement* **15**(6), 840–858 (2019).
12. Heye, A. K. et al. Assessment of blood-brain barrier disruption using dynamic contrast-enhanced MRI. *Syst. Rev. Neuroimage Clin.* **6**, 262–274 (2014).
13. Manning, C. et al. Sources of systematic error in DCE-MRI estimation of low-level blood-brain barrier leakage. *Magn. Reson. Med.* **86**(4), 1888–1903 (2021).
14. Wong, S. M. et al. Measuring subtle leakage of the blood-brain barrier in cerebrovascular disease with DCE-MRI: Test-retest reproducibility and its influencing factors. *J. Magn. Reson. Imaging.* **46**(1), 159–166 (2017).
15. Zhu, G. et al. Comparison of MRI IVIM and MR perfusion imaging in acute ischemic stroke due to large vessel occlusion. *Int. J. Stroke* **15**(3), 332–342 (2020).
16. Hales, P. W. & Clark, C. A. Combined arterial spin labeling and diffusion-weighted imaging for noninvasive estimation of capillary volume fraction and permeability-surface product in the human brain. *J. Cereb. Blood Flow Metab.* **33**(1), 67–75 (2013).
17. Selya, A. S. et al. A Practical Guide to Calculating Cohen's f(2), a Measure of Local Effect Size, from PROC MIXED. *Front Psychol.* **3**, 111 (2012).
18. Le Bihan, D. What can we see with IVIM MRI?. *Neuroimage* **187**, 56–67 (2019).
19. Sun, J. et al. The relationship between microvasculature in white matter hyperintensities and cognitive function. *Brain Imaging Behav.* **11**(2), 503–511 (2017).
20. Wong, S. M. et al. Simultaneous investigation of microvasculature and parenchyma in cerebral small vessel disease using intravoxel incoherent motion imaging. *Neuroimage Clin.* **14**, 216–221 (2017).
21. Paschoal, A. M. et al. Contrast-agent-free state-of-the-art MRI on cerebral small vessel disease-part 1. ASL, IVIM, and CVR. *NMR Biomed.* https://doi.org/10.1002/nbm.4742 (2022).

22. Kerkhofs, D. et al. Baseline Blood-Brain Barrier Leakage and Longitudinal Microstructural Tissue Damage in the Periphery of White Matter Hyperintensities. *Neurology* **96**(17), e2192–e2200 (2021).
23. Liesche-Starnecker, F. et al. Visualizing cellularity and angiogenesis in newly-diagnosed glioblastoma with diffusion and perfusion MRI and FET-PET imaging. *EJNMMI Res.* **11**(1), 72 (2021).
24. Bahrani, A. A. et al. White Matter Hyperintensity Associations with Cerebral Blood Flow in Elderly Subjects Stratified by Cerebrovascular Risk. *J. Stroke Cerebrovasc. Dis.* **26**(4), 779–786 (2017).
25. Markus, H. et al. Reduced cerebral blood flow in white matter in ischaemic leukoaraiosis demonstrated using quantitative exogenous contrast based perfusion MRI. *J. Neurol. Neurosurg. Psychiatry* **69**(1), 48–53 (2000).
26. Promjunyakul, N. et al. Characterizing the white matter hyperintensity penumbra with cerebral blood flow measures. *Neuroimage Clin* **8**, 224–229 (2015).
27. Promjunyakul, N. O. et al. Comparison of cerebral blood flow and structural penumbras in relation to white matter hyperintensities: A multi-modal magnetic resonance imaging study. *J. Cereb. Blood. Flow Metab.* **36**(9), 1528–1536 (2016).
28. Li, Q. et al. Cerebral Small Vessel Disease. *Cell Transplant.* **27**(12), 1711–1722 (2018).
29. Brown, W. R. & Thore, C. R. Review: Cerebral microvascular pathology in ageing and neurodegeneration. *Neuropathol. Appl. Neurobiol.* **37**(1), 56–74 (2011).
30. Lowerison, M. R. et al. Aging-related cerebral microvascular changes visualized using ultrasound localization microscopy in the living mouse. *Sci. Rep.* **12**(1), 619 (2022).
31. Sun, Z. et al. In Vivo Detection of Age-Related Tortuous Cerebral Small Vessels using Ferumoxytol-enhanced 7T MRI. *Aging Dis.* **15**(4), 1913–1926 (2024).
32. Kadry, H., Noorani, B. & Cucullo, L. A blood-brain barrier overview on structure, function, impairment, and biomarkers of integrity. *Fluids Barriers CNS* **17**(1), 69 (2020).
33. Wardlaw, J. M., Benveniste, H. & Williams, A. Cerebral Vascular Dysfunctions Detected in Human Small Vessel Disease and Implications for Preclinical Studies. *Annu. Rev. Physiol.* **84**, 409–434 (2022).
34. Inoue, Y. et al. Pathophysiology and probable etiology of cerebral small vessel disease in vascular dementia and Alzheimer's disease. *Mol. Neurodegener.* **18**(1), 46 (2023).
35. Zhang, C. E. et al. Blood-brain barrier leakage in relation to white matter hyperintensity volume and cognition in small vessel disease and normal aging. *Brain Imaging. Behav.* **13**(2), 389–395 (2019).
36. Li, Y. et al. Decreased water exchange rate across blood-brain barrier in hereditary cerebral small vessel disease. *Brain* **146**(7), 3079–3087 (2023).
37. Ter Telgte, A. et al. Cerebral small vessel disease: from a focal to a global perspective. *Nat. Rev. Neurol.* **14**(7), 387–398 (2018).
38. Hannawi, Y. Cerebral Small Vessel Disease: a Review of the Pathophysiological Mechanisms. *Transl. Stroke Res.* **15**(6), 1050–1069 (2024).
39. Neumann, K. et al. Microvascular Impairment in Patients With Cerebral Small Vessel Disease Assessed With Arterial Spin Labeling Magnetic Resonance Imaging: A Pilot Study. *Front Aging Neurosci.* **14**, 871612 (2022).
40. Nurnberger, L. et al. Longitudinal changes of cortical microstructure in Parkinson's disease assessed with T1 relaxometry. *Neuroimage Clin.* **13**, 405–414 (2017).
41. Dai, W., Shankaranarayanan, A. & Alsop, D. C. Volumetric measurement of perfusion and arterial transit delay using hadamard encoded continuous arterial spin labeling. *Magn. Reson Med.* **69**(4), 1014–1022 (2013).
42. Ashburner, J. & Friston, K. J. Unified segmentation. *Neuroimage* **26**(3), 839–851 (2005).
43. Le Bihan, D. et al. MR imaging of intravoxel incoherent motions: application to diffusion and perfusion in neurologic disorders. *Radiology* **161**(2), 401–407 (1986).
44. Li, K. L. et al. Four-phase single-capillary stepwise model for kinetics in arterial spin labeling MRI. *Magn. Reson Med.* **53**(3), 511–518 (2005).
45. Gulati, G. et al. Altered Blood-Brain Barrier Permeability in Patients With Systemic Lupus Erythematosus: A Novel Imaging Approach. *Arthritis Care Res. (Hoboken)* **69**(2), 299–305 (2017).
46. Whitfield-Gabrieli, S. & Nieto-Castanon, A. Conn: a functional connectivity toolbox for correlated and anticorrelated brain networks. *Brain Connect* **2**(3), 125–141 (2012).
47. Van Essen, D. C. et al. The Human Connectome Project: A data acquisition perspective. *Neuroimage* **62**(4), 2222–2231 (2012).

Acknowledgements

L.W. discloses support for the research of this work from a University of Cincinnati Gardener Neuroscience Institute pilot grant.

Author contributions

LW: study conception, study oversight, design, data acquisition, results interpretation, manuscript preparation, BW: study conception, design, MRI protocol, data acquisition, data analysis, results interpretation, manuscript preparation, BZ: statistical consultation, data analysis, AS: data acquisition, manuscript preparation, YA: design, data acquisition, results interpretation, EA: design, data acquisition, CS: data acquisition, manuscript preparation, AV: study conception, results interpretation, PK: study conception, results interpretation, MD: study conception, design, MRI protocol, data acquisition, data analysis, results interpretation, manuscript preparation. All authors engaged in manuscript review.

Declarations

Competing interests

The authors declare no competing interests.

Additional information

Correspondence and requests for materials should be addressed to M.W.D.